Mechanical Systems and Signal Processing 149 (2021) 107298

Contents lists available at ScienceDirect

Mechanical Systems and Signal Processing

journal homepage: www.elsevier.com/locate/ymssp

A theoretical-experimental framework for the analysis of the dynamic response of a QEPAS tuning fork device immersed in a fluid medium

Angelo Campanale [a], Carmine Putignano [a,*], Simone De Carolis [a], Pietro Patimisco [b], Marilena Giglio [b], Leonardo Soria [a]

[a] Department of Mechanics, Mathematics and Management, Politecnico di Bari, Bari, Italy
[b] PolySense Lab – Dipartimento Interateneo di Fisica, University and Politecnico of Bari, CNR-IFN, Via Amendola 173, Bari, Italy

ARTICLE INFO

Article history:
Received 1 March 2020
Received in revised form 13 July 2020
Accepted 9 September 2020

Keywords:
Quartz-enhanced photoacoustic spectroscopy
Quartz tuning fork
Boundary element methods
Fluid-structure interaction
Vibroacoustic analysis

ABSTRACT

Quartz-enhanced photoacoustic spectroscopy (QEPAS) is a trace gas sensing technique that employs a designed high-quality factor quartz tuning fork (QTF) as acousto-electric transducer. The first in-plane skew-symmetric flexural mode of the QTF is excited when weak resonant sound waves are generated between the QTF prongs. Thus, the performance of a QEPAS sensor strongly depends on the resonance properties of the QTF, namely the determination of flexural eigenfrequencies and air damping loss.

In this work, we present a mixed theoretical-experimental framework to study the dynamic response of a QTF while vibrating in a fluid environment. Due to the system linearity, the dynamic response of the resonator immersed in a fluid medium is obtained by employing a Boundary Element formulation based on an *ad hoc* calculated Green's function. In particular, the QTF is modelled as constituted by a pair of two Euler-Bernoulli cantilevers partially coupled by a distributed linear spring. As for the forces exerted by the fluid on QTF structure, the fluid inertia and viscosity as well as an additional diffusivity term, whose influence is crucial for the correct evaluation of the system response, have been taken into account.

By corroborating the theoretical analysis with the experimental outcomes obtained by means of a vibro-acoustic setup, the fluid response coefficients and the dynamics of the QTF immersed in a fluid environment are fully determined.

1. Introduction

The sensitive and selective detection of trace gas concentrations has found widespread applications [1], and includes several fields, such as environmental monitoring [2], industrial process control [3], rural and urban emission studies [4], chemical analysis and control of manufacturing processes [5]. Numerous analytical instruments based on optical and non-optical techniques have been developed with the aim to offer high sensitivity and selectivity, multicomponent detection capability, room temperature operation, fast response time, large dynamic range, and ease of use [6].

* Corresponding author. Tel./Fax.: +390805963512.
E-mail address: carmine.putignano@poliba.it (C. Putignano).

https://doi.org/10.1016/j.ymssp.2020.107298
0888-3270/

Optical techniques based on tunable laser absorption spectroscopy (TDLAS) for trace gas sensing are not far from being able to meet these requirements. Among them, photoacoustic spectroscopy (PAS) has established as a very attractive technique for sensitive trace gas detection [6]. It is based on the photoacoustic effect [7,8], i.e. on the generation of sound waves as a consequence of the absorption of modulated light by a target gas. PAS uses resonant cells to enhance the acoustic wave and sensitive microphones to detect and transduce it into an electric signal [9,10]. Thus, PAS does not require an optical detector and the detection scheme is wavelength-insensitive.

Since 2002 [11,12], Quartz-Enhanced PAS (QEPAS) has been proposed as a variant of traditional PAS: the acoustic cells are, in this case, replaced by small quartz tuning forks (QTFs), acting as sharply resonant acoustic transducers to detect weak photoacoustic excitation. The employment of a QTF allowed size reduction of the acoustic detection unit as well as high immunity, during operation, to environmental noise caused by external excitation sources, owing to the reduction of the detection bandwidth due to the high quality factor of the QTF resonance. Therefore, QEPAS technology is competitive with and, in many cases, preferred to other trace gas sensing methods [13–17].

Looking at its mechanical structure, a QTF can be considered as two cantilevers (prongs) joined at a common base. The in-plane flexural modes of vibrations of the QTFs can be classified into two groups: symmetrical modes, where the prongs moves along the same direction, and anti-symmetrical modes, where the two prongs oscillate along opposite directions [18,19]. The in-plane anti-symmetrical modes are the predominant ones when a sound source is positioned between the prongs, forcing them to move in the opposite directions. In QEPAS sensors, as shown in the schematic in Fig. 1, the light source is focused between the QTF prongs and the sound waves produced by the modulated absorption of the gas are generated between the QTF prongs, forcing them to vibrate anti-symmetrically back and forward. A schematic of the core of a QEPAS sensor is sketched in Figure 1. Thus, in-plane anti-symmetrical modes of the QTF are excited. When these oscillations occur at one of the resonance frequencies of the QTF, the induced strain field generates surface electric charges due to the quartz piezoelectricity and the total charge is proportional to the intensity of the sound waves incident on the QTF prongs. The generated charges are collected using a transimpedance amplifier and the measured electrical signal is proportional to the concentration of absorbing gas species.

As a consequence, the performance of a QEPAS sensor is strongly determined by the resonance properties of the QTF, which is fully immersed in the gas sample. Thus, it is crucial to study the response of the QTF in a fluid medium while it is vibrating, at the in-plane anti-symmetrical flexural mode. Several theoretical models describing the main loss mechanisms, namely the air damping [26–28], support losses [27,29–31] and thermoelastic damping [32] have been proposed for a single cantilever oscillating in fluid medium or in vacuum. These models have been applied to a QTF to predict dependence of the quality factor on the QTF prong geometry, for both the fundamental and first overtone flexural mode [33,34]. While the trends are well predicted, QTF overall quality factor values are poorly estimated. Besides, when assuming fixed the base plate and neglecting the coupling between the two prongs, an excellent estimation of the in-plane flexural eigenfrequencies can be obtained only as long as the QTF prongs are slender beams [22]. Conversely, for QTF geometry with squat prongs, neglecting the vibration of the base plate and its coupling effect can lead to incorrect estimation of the eigenfrequencies. For this reason, the effect of the base plate, as vibrating and structural coupling element, has to be considered [20].

In this work, we propose a theoretical-experimental model to determine the response of the QTF vibrating in a fluid medium in a relatively simple and phenomenological way. As a consequence, this approach will provide more control on the governing parameters of the physical phenomenon: these will be easily recognized, controlled, and optimized, and without using computational-demanding fluid-structure interaction numerical simulations [48]. Specifically, the proposed model employs a combined analytical-experimental methodology to analyze the dynamic response of a quartz tuning fork when forced to vibrate to the fundamental anti-symmetrical flexural mode, by accounting for the effects due to the interaction with the surrounding fluid. Due to its linearity, the system response is calculated by using an *ad hoc* Green's function. The system domain includes two Euler-Bernoulli beams partially coupled by a distributed linear spring [35], used to model the plate connecting the two prongs as well as the underlying part. The drag force exerted by the fluid on the QTF is modelled

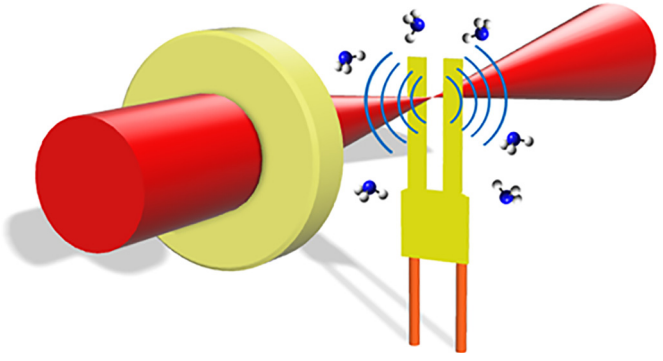

Fig. 1. QEPAS principle of operation. A QTF is immersed in a fluid and laser light is focused between two QTF prongs. Weak sound waves generated by photoacoustic effect deflect the prong in two opposite directions.

by a simple integral expression which accounts not only for fluid inertia and viscosity but also for a diffusivity vorticity term [42–44], whose influence is fundamental for the correct evaluation of the system response [47].

As usually done for many applications in solid mechanics [50–53], in the framework of the Boundary Element Methodology (BEM) [49], the problem is reduced to the solution of an integral equation between forces and displacements.

Once the theoretical expression of the system response is determined, an experimental test on a specific QTF vibrating in air was performed to fine tune the theoretical response. An acoustic stationary random field generated by two speakers has been used to excite the QTF and the resulting forced vibration time series has been measured and recorded by using a LD vibrometer, while an electronic microphone has been employed to measure the acoustic pressure in a specific point close to the QTF.

The paper is organized as follows: in Section 2, the mathematical model is presented, with a description of the QTF dynamics and its interaction with the surrounding fluid with an analysis on the stochastic excitation source used in the experiments; in Section 3, the experimental setup is described; in Section 4, the theoretical model is fitted on the experimental data and the effect of the diffusivity fluid term as well as the structural coupling term are discussed; in Section 5, final remarks are provided. In Appendix A, the calculation of the Green's function of the QTF is reported and the relative boundary conditions are provided; finally, Appendix B includes fluid dynamics Finite Element calculations to estimate the hydrodynamic function's coefficients.

2. Mathematical model formulation

2.1. Dynamics equations

In this section, the mathematical model describing the in-plane flexural vibration of a quartz tuning fork (QTF) device immersed in a viscous fluid is presented. The structure is split into four parts, each modelled as a one-dimensional (1D), linear Euler-Bernoulli beam with a rectangular cross section of thickness h. The underlying two beams are considered coupled by a set of distributed linear springs with constant stiffness per unit length k, as represented in Figure 2. Specifically, the two interconnected beams, labelled as BL (bottom-left) and BR (bottom-right), having width $B/2$ and length L_b, model the base plate of the QTF; the beams labelled as TL (top-left) and TR (top-right), with width $b$and length L_p, model the two prongs of the tuning fork. Beams BL and TL and beams BR and TR are, respectively, segments of two cantilevers with length $L = L_b + L_p$, each having a step discontinuity on the cross section. Their dynamics is governed by the following motion equation

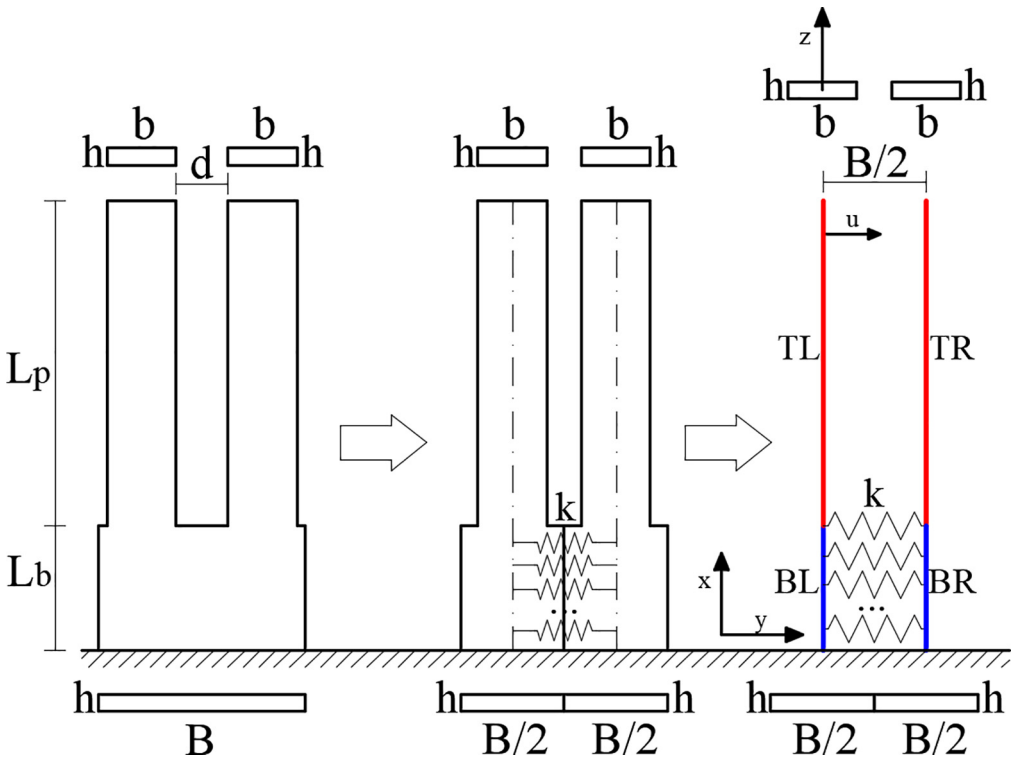

Fig. 2. Reduction of the 3D QTF to a 1D Euler-Bernoulli model.

$$EJ(x)\frac{\partial^4 u_i(x,t)}{\partial x^4}+\rho A(x)\frac{\partial^2 u_i(x,t)}{\partial t^2}+k(x)\big(u_i(x,t)-u_j(x,t)\big)=f_i(x,t) \tag{1}$$

where t is the time variable, x is the common coordinate along the beam axes, with y and z the coordinates along the width and thickness directions, respectively. Furthermore, $u_i(x,t)$ and $u_j(x,t)$ indicate the in-plane elastic deflection of the i-th and j-th cantilever, respectively, with $i,j=1,2$ and $i\neq j$; ρ and E are the mass per unit volume and the Young's modulus of the material of the beams, respectively. Finally, we have $A(x)=A_b-\mathcal{H}(x-L_b)(A_b-A_p)$, with $\mathcal{H}(x)$ the Heaviside unit step function, $A_b=hB/2$ and $A_p=hb$ the cross-section areas of the bottom and top segments, respectively, $J(x)=J_b-\mathcal{H}(x-L_b)(J_b-J_p)$, with $J_b=h(B/2)^3/12$ and $J_p=hb^3/12$ the corresponding inertia moments; the coupling stiffness $k(x)$ is equal to $k(1-\mathcal{H}(x-L_b))$. The forcing term $f_i(x,t)$ is equal to $f_i^{ext}(x,t)+f_i^F(x,t)$, where $f_i^{ext}(x,t)$ is the overall external force per unit length acting on the i-th beam, not including the contribution $f_i^F(x,t)$, exerted by the encompassing fluid, that we assume to be Newtonian and incompressible.

The boundary conditions to be taken into account for each cantilever are the well-known fixed-free boundary conditions, that is $u_i(0,t)=0,\partial u_i(0,t)/\partial x=0,\partial^2 u_i(L,t)/\partial x^2=0,\partial^3 u_i(L,t)/\partial x^3=0$.

2.2. Fluid-Structure Interaction

Assuming small in-plane deflections, the fluid response can be considered linear and the force $f_i^F(x,t)$ can be evaluated by means of the following Green's function approach [47]

$$f_i^F(x,t)=\int_{-\infty}^{t}\int_0^L d\tau dx' G_F(x,x',t-\tau)\frac{\partial u_i^2(x',\tau)}{\partial \tau^2} \tag{2}$$

where the form of $G_F(x,x',t)$ is heuristically derived. Specifically, by assuming $L\gg b$ and $b\gg h$, we are allowed to neglect the three-dimensional (3D) phenomena related to variations of the flow physics along the beams' axes, as we assimilate the beams' cross-sections to rigid slender bodies. Thus, the hydrodynamic loading per unit length can be estimated by studying the two-dimensional (2D) flow induced by the small amplitude oscillations of those bodies in the transversal direction [38,36,37,39–41]. Thus, the fluid response can be modelled as $G_F(x,x',t)=G_F(x,t)\delta(x-x')$, rephrasing accordingly Equation (2) as

$$f_i^F(x,t)=\int_{-\infty}^{t} d\tau G_F(x,t-\tau)\frac{\partial u_i^2(x,\tau)}{\partial \tau^2} \tag{3}$$

In this way, it is possible to study the unsteady Stokes' flow generated by the linear oscillation of an isolated slender body, governed by the following equations

$$\frac{\partial \mathbf{W}}{\partial t}=\nu\nabla^2\mathbf{W} \tag{4}$$

$$\nabla\cdot\mathbf{v}=0 \tag{5}$$

where ∇ and ∇^2 are the Nabla and Laplace operators. Equation (4) represents the linearized momentum equation, expressed in form of vorticity $\mathbf{W}=\nabla\times\mathbf{v}$ [44], while Equation (5) is the continuity equation, with $\mathbf{v}$ and ν the velocity and the kinematic viscosity of the fluid, respectively.

As the vorticity is governed by a diffusive-like equation, it generates a solution in terms of velocity that exponentially decays from the boundary of the body toward the interior fluid. The amplitude of this exponential decays allows the estimation of the thickness h_f of the fluid layer, where the fluid behaves as rotational and the diffusion of the tangential velocity is important. Let us notice that $h_f\approx\sqrt{\nu/\omega}$, where ω is the characteristic radian frequency of the motion. Outside of the layer, the term $\nu\nabla^2\mathbf{W}$ can be neglected and a potential flow is established.

Since h_f is frequency-dependent, it is very small in the high frequency range, with the fluid response solely governed by inertial effects and, thus, proportional to the acceleration of the moving body. In this case, the Green's function of the fluid has to be proportional to the Dirac Delta function $\delta(t)$ by means of a certain inertia coefficient $\mu(x)$. Conversely, at low frequencies, the Eulerian rate of change $\partial\mathbf{W}/\partial t$ can be neglected and h_f becomes larger than the characteristic dimensions of the moving body. In this case, the fluid response is expected to be linearly proportional to the body velocity, implying a form of the fluid Green's function proportional to a specific damping coefficient $c(x)$. In the mid frequency range, the effects of vorticity diffusion are predominant [44]. Thus, in this latter case, the fluid Green's function has to come inversely proportional to $\sqrt{t}$, by a particular diffusive coefficient $\alpha(x)$.

In conclusion, due to the linearity of the sought fluid response, the overall force exerted by the fluid on the oscillating body has to be the sum of those three contributions

$$\begin{aligned} &G_F(x,t)=-c(x)-\tfrac{\alpha(x)}{\sqrt{t}}-\mu(x)\delta(t)\quad t\geqslant 0\\ &G_F(x,t)=0\quad t<0\end{aligned} \tag{6}$$

Equation (6), which satisfies the causality principle, clearly is an heuristic approximation of the fluid response. Furthermore, the dependence of the three fluid coefficients on the spatial abscissa x is negligible in the case of an isolated cantilever vibrating in an unbounded fluid [47], as in the case considered in the present study. To estimate the numerical values assumed by the three coefficients in our application, the best fit of the experimental response has to be performed.

By substituting Equation (6) in Equation (3), the following expression of the exerted fluid force is obtained

$$f_i^F(x,t) = -c\frac{\partial u_i(x,t)}{\partial t} - \alpha\int_{-\infty}^{t} d\tau \frac{1}{\sqrt{t-\tau}}\frac{\partial u_i^2(x,\tau)}{\partial \tau^2} - \mu\frac{\partial u_i^2(x,t)}{\partial t^2} \tag{7}$$

Equation (7) can be transformed from time to Laplace domain with $s = \mathrm{i}\omega$, where s the Laplace variable, $\mathrm{i} = \sqrt{-1}$, $\omega = 2\pi\,\mathrm{f}$ with f the time frequency, and, so that, $\hat{u}_i(x,s) = \int_0^{+\infty} dt\, u_i(x,t)\,\mathrm{e}^{-st}$. Ultimately, it is possible to define

$$\hat{f}_i^F(x,\omega) = \omega^2\Gamma(\omega)\hat{u}_i(x,\omega) \tag{8}$$

where

$$\Gamma(\omega) = \mu + \alpha\sqrt{\frac{\pi}{2}}\omega^{-1/2} - \mathrm{i}\left(c\omega^{-1} + \alpha\sqrt{\frac{\pi}{2}}\omega^{-1/2}\right) \tag{9}$$

is the so-called hydrodynamic function [38–41], whose real part describes the fluid added mass, while the imaginary part accounts for the hydrodynamic damping.

The diffusive-velocity contribution, proportional to the α coefficient, gives rise to two identical terms appearing symmetrically in the real and imaginary parts of $\Gamma(\omega)$, implying that this contribution equally influences both the added mass and the hydrodynamic damping, and, in turn, both the eigenfrequencies and the quality factors associated to system eigenmodes. The overall mass adding effect can be neglected, as also reported in literature (see Refs. [1–33]), in the case of QEPAS applications, and in Refs. [45,46], in the case of the laterally vibrating microcantilevers; while a correct estimation of the hydrodynamic damping is crucial, since the QTF quality factor plays a fundamental role in design and operation of those resonators. Indeed, at atmospheric pressure the fluid damping is the dominant energy dissipation mechanism [22]–[33,34] and any form of inner structural dissipation can be neglected.

Let us now focus more in detail on the key feature marking the hydrodynamic function $\Gamma(\omega)$, that is, the presence of the diffusive velocity term in the description of the fluid force exerted on the structure. Specifically, by accounting for this term, it is possible to consider the effects of the tangential velocity diffusion, going from the fluid layer, adhering to the skin of each beam, towards the interior part of the fluid region. From a physical point of view, this has a crucial importance as it can be understood by focusing on a very simple model. Indeed, let us consider the case of a Newtonian, incompressible and viscous fluid bounded by an infinite plane surface, which executes small oscillation in its own plane. In particular, the solid surface is placed in the xy-plane, the fluid region coincides with the half-space for $z > 0$, the direction of the surface oscillation is taken in the y-axis and the time law of the surface motion is given by $u(t) = u_0 e^{-i\omega t}$. In this specific case, the motion of the fluid is governed by a purely 1D diffusive equation [44]

$$\rho\frac{\partial v_y}{\partial t} = \eta\frac{\partial^2 v_y}{\partial y^2} \tag{10}$$

where v_y is the fluid velocity in the y-direction. Such an infinite planar surface oscillating in a viscous fluid, fits perfectly the conditions of the device under study in this paper, i.e. the QTF#S15, whose dimensions are listed in Table 1. Indeed, each single prong can be approximated to a flat plate moving in a viscous fluid. Furthermore, with the regards to the role of diffusion in Eq. (9), it is well known in literature that, apart from the added mass constant, terms depending on $\omega^{-1/2}$ of both real and imaginary part of $\Gamma(\omega)$ are arguably, in the frequency range of interest, the leading ones in a series expansion of the hydrodynamic function. This has been demonstrated, for example, in Ref. [38] for the out-of-plane motion in fluid of a single microcantilever and in Ref. [45,46] for its in-plane motion; a similar scaling effect has to be considered in the case of the hydrodynamic coupling of two microcantilevers, as shown in Ref [39].

Table 1
Dimensions of the QTF#S15 device used in this work, the nomenclature refers to Fig. 2.

QTF#S15 Dimensions [mm]	
Prong Length	$L_p = 9.4$
Base Length	$L_b = 3.6$
Prong Width	$b = 2$
Base Width	$B = 6$
Prong Spacing	$d = 1.5$
QTF Thickness	$h = 0.25$

Ultimately, these considerations suggest that it is possible to neglect the contribution of the viscous term c and obtain a simplified expression of the hydrodynamic function, as

$$\Gamma(\omega) = \mu + (1 - \mathrm{i})\alpha\sqrt{\frac{\pi}{2}}\omega^{-1/2} \tag{11}$$

A more detailed analysis on the estimation of the hydrodynamic function's coefficients, on the dominance of the diffusive term, and on the negligible effect of mass adding can be found in Appendix B, where these considerations are corroborated by a CFD analysis. Specifically, we there show that $c\omega^{-1} \ll \alpha\sqrt{\pi/2\omega}$ and that the whole real part of $\Gamma(\omega)$ can be neglected when compared to the cantilevers' mass per unit length, that is $\mu + \alpha\sqrt{\pi/2\omega} \ll \rho A(x)$.

2.3. Dynamics equations in the frequency domain

By rephrasing the motion equations of the two cantilevers (1) in the frequency domain, accounting for Equation (8) and adopting a suitable matrix notation, the following compact description of the QTF dynamics can be obtained

$$\frac{\partial^4 \bar{u}(x,\omega)}{\partial x^4} + \bar{\bar{B}}(x,\omega)\bar{u}(x,\omega) = \bar{f}^{ext}(x,\omega) \tag{12}$$

where $\bar{u}(x,\omega) = \{\hat{u}_1(x,\omega), \hat{u}_2(x,\omega)\}^{\mathrm{T}}$, $\bar{f}^{ext}(x,\omega) = (1/EJ(x))\left\{\hat{f}_1^{ext}(x,\omega), \hat{f}_2^{ext}(x,\omega)\right\}^{\mathrm{T}}$, in which T denotes matrix transposition, and

$$\bar{\bar{B}}(x,\omega) = \begin{bmatrix} B(x,\omega) & -\frac{k(x)}{EJ(x)} \\ -\frac{k(x)}{EJ(x)} & B(x,\omega) \end{bmatrix}$$

with $B(x,\omega) = (1/EJ(x))\left(-\omega^2(\rho A(x) + \Gamma(\omega)) + k(x)\right) \approx (1/EJ(x))\left(-\omega^2\left(\rho A(x) - \mathrm{i}\alpha\sqrt{\pi/2\omega}\right) + k(x)\right)$, since, as anticipated, $c\omega^{-1} \ll \alpha\sqrt{\pi/2\omega}$ and $\mu + \alpha\sqrt{\pi/2\omega} \ll \rho A(x)$.

The fluid coupling between the prongs is neglected in the QTF dynamics modelled by the set of Equations (12). In fact, on the one hand, being the QEPAS technique a gas sensing application, the densities of operated fluids are at least 3 order of magnitude lower than the density of the QTF material, i.e. quartz. On the other hand, the prongs' spacing is comparable to the prongs' width and it is several times larger than the prongs' thickness. With QTF#S15, investigate in this work, the spacing-to-width ratio is equal to 0.75, while the spacing-to-thickness ratio is equal to 6 (see Table 1).

2.4. Computation of the linear response

By relying on the linearity of system's Equations (12), a Green's function approach has been adopted to determine the specific solution of the problem. Hence, the system's complex Green's function is calculated, even referred to the susceptibility function, which is the solution of the so-called fundamental problem [47]. Specifically, a concentrated force of unit impulse is supposed to be applied to a generic cross-section ξ of the resonator (Figure 3), that is, to a certain section ξ of the j-th cantilever, when the other remains unloaded. The output of the i-th cantilever when the system is subjected to such a loading condition of this kind [21] is denoted with $G_{ij}(x,\xi,\omega)$, as depicted in Figure 3. Details on the computation are reported in Appendix A.

Then, the in-plane elastic deflection of each cantilever, caused by a generic load $\bar{f}(x,\omega)$ acting on the system, is calculated by means of the following integral equation

$$\hat{u}_i(x,\omega) = \int_0^L d\xi\, G_{ii}(x,\xi,\omega)\hat{f}_i(\xi,\omega) + \int_0^L d\xi\, G_{ij}(x,\xi,\omega)\hat{f}_j(\xi,\omega) \tag{13}$$

where $i,j = 1,2$ and $i \neq j$.

We observe that the susceptibility function $G_{ij}(x,\xi,\omega)$ is function of the fluid coefficient α as well as of the coupling stiffness k, whose numerical values can be found by tuning the model with experimental outcomes. The experimental response will be fitted in correspondence to the first skew-symmetric in-plane flexural mode, which is the piezoelectrically active mode of QTFs typically employed in QEPAS applications. For QTF#S15, it falls at 15.808 kHz. In Figure 4, the magnitude and the phase angle of the susceptibility functions of both cantilevers are reported, evaluated at their tips $x = L$, while the concentrated force is applied to the half-length of the base $\xi = L_b/2$ of the left cantilever. We notice that the two prongs vibrate out of phase, as expected in the case of the first skew-symmetric in-plane flexural mode.

In order to calculate the susceptibility functions $G_{ij}(x,\xi,\omega)$ accounting for the system boundary conditions, the solution of the fundamental problem is obtained in a discrete form (details are reported in Appendix A).

Then, these susceptibility functions are stored in a matrix form by adopting the following numerical procedure: (i) discretize the interesting range of frequencies ω_k with N_k points and the spatial abscissas x_r and ξ_s with N points along the total cantilever length L, thus defining the spatial discretizations as $\Delta x = \Delta\xi = L/(N-1)$, (ii) apply, for fixed value of ω_k, a concen-

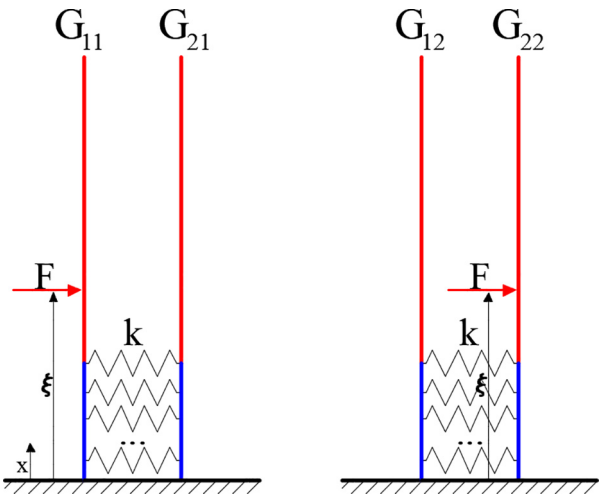

Fig. 3. Susceptibility function adopted notation. The susceptibility function comprises $G_{11}(x,\xi,\omega)$ and $G_{21}(x,\xi,\omega)$ in the case the unit impulse concentrated force is applied to a generic section ξ of the left cantilever while the right one remains unloaded (left panel); $G_{12}(x,\xi,\omega)$ and $G_{22}(x,\xi,\omega)$ in the case the load is exerted on a section ξ of the right cantilever with the left unforced (right panel).

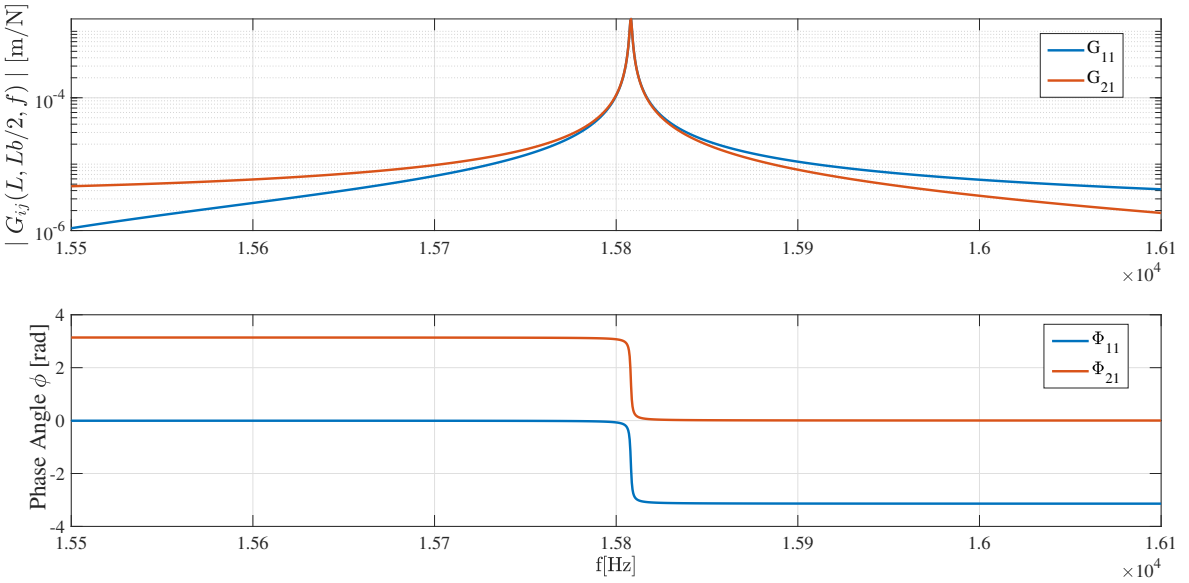

Fig. 4. Magnitudes and phase angles of susceptibility functions $G_{11}(L,L_b/2,\omega)$ (blue curve) and $G_{21}(L,L_b/2,\omega)$ (red curve) of the two cantilevers of QTF#S15, computed by employing as coefficients $\alpha = 2.341\times10^{-5}\text{Pa s}^{3/2}$ and $k = 1.7865\times10^{9}\text{Pa}$. (For interpretation of the references to colour in this figure legend, the reader is referred to the web version of this article.)

trated load at a generic section ξ_s of a single cantilever and compute the quantities $G_{ij}(x_r,\xi_s,\omega_k)$ for $i,j=1,2$, by solving the fundamental problem, (iii) repeat the previous step for all the ω_k values included in the chosen frequency range.

By following this procedure, the matrices $[\boldsymbol{G}]_{ij}$ for both cantilevers are obtained

$$[\mathbf{G}]_{ij} = \left[G_{ij}(x_r,\xi_s,\omega_k)\right] \tag{14}$$

with $i,j=1,2,\ r=1,\dots,N,\ s=1,\dots,N$, and $k=1,\dots,N_k$. It is worth noting that, for a fixed frequency, a column of the $[\mathbf{G}]_{ij}$ matrix represent the in-plane elastic deflection of the system when a concentrated load is applied to a generic section.

Now, the global susceptibility matrix $\bar{\bar{\boldsymbol{G}}}$ can be defined as

$$\bar{\bar{\boldsymbol{G}}} = \begin{bmatrix} [\boldsymbol{G}]_{11} & [\boldsymbol{G}]_{12} \\ [\boldsymbol{G}]_{21} & [\boldsymbol{G}]_{22} \end{bmatrix} \tag{15}$$

where, due to the symmetry of the problem, $[\boldsymbol{G}]_{11}$ is equal to $[\boldsymbol{G}]_{22}$ and $[\boldsymbol{G}]_{12}$ is equal to $[\boldsymbol{G}]_{21}$.

The load vector $\bar{\boldsymbol{F}}$ and the displacement vector $\bar{\boldsymbol{U}}$ are defined as

$$\bar{\boldsymbol{F}} = \begin{Bmatrix} \{\boldsymbol{F}\}_1 \\ \{\boldsymbol{F}\}_2 \end{Bmatrix} \quad \bar{\boldsymbol{U}} = \begin{Bmatrix} \{\boldsymbol{U}\}_1 \\ \{\boldsymbol{U}\}_2 \end{Bmatrix} \tag{16}$$

with $\{\boldsymbol{F}\}_i = \left\{\hat{f}_i(\xi_s, \omega_k)\Delta\xi\right\}$ for $i = 1, 2$, $s = 1, \ldots, N$, and $k = 1, \ldots, N_k$; and $\{\boldsymbol{U}\}_i = \left\{\widehat{U}_i(x_r, \omega_k)\right\}$ for $i = 1, 2$, $r = 1, \ldots, N$, and $k = 1, \ldots, N_k$. Therefore, it is possible to describe the in-plane displacement of each cantilever in a convenient matrix form as a canonical BEM formulation for a fixed value of temporal frequency ω_k, as

$$\bar{\boldsymbol{U}} = \bar{\bar{\boldsymbol{G}}}\bar{\boldsymbol{F}} \tag{17}$$

Equation (17) is the discrete version of integral Equation (13) and correlates displacements with loads by means of the global response matrix of the system.

2.5. Analysis of the excitation sources

As final analysis, a study of the QTF dynamic response to distributed forces that are non-deterministic in nature, both in time and space, is presented. In fact, this is the input kind acting on the QTF device during the experiments, in which, as anticipated, two acoustic speakers are used as excitation sources for generating a white, random acoustic field.

The external force per unit length on both the cantilevers have been modelled, in the form of the product of two ergodic, Dirac-Delta-correlated terms, respectively describing the time and space unpredictable behaviour of the external excitation.

The spatial behaviour of the random loading acting on a single cantilever of the QTF can be described, in a discrete form, by the following autocorrelation matrix

$$\bar{\bar{\mathbf{C}}}_{X,i} = \bar{\bar{\mathbf{C}}}_X = S_X^{(0)}\bar{\bar{\mathbf{I}}} \tag{18}$$

with $i = 1, 2$, $\bar{\bar{\mathbf{I}}}$ a N X N identity matrix and the intensity of the spatial part of the stochastic load $S_X^{(0)}$ defined as

$$S_{X,i}(q) = S_X^{(0)} = \frac{< \left|\widehat{X}_i(q)\right|^2 >}{L} \tag{19}$$

where q indicates the radian spatial frequency, $\widehat{X}_i(q)$ is the single realization of the spatial stochastic loading acting on each cantilever and is equal to $\sqrt{S_X^{(0)}}\mathrm{e}^{\mathrm{i}\phi_{X,i}(q)}$, with $\phi_{X,i}(q)$ random phases uniformly distributed in the range from $-\pi$ to π. In Eq. (19), we assume the same intensity of spatial stochastic noise for both cantilevers $S_{X,1}^{(0)} = S_{X,2}^{(0)} = S_X^{(0)}$.

A unique scalar coefficient $S_T^{(0)}$, indicating the intensity of the temporal part of the stochastic load, is requested to describe the temporal behaviour of the random loading, owing to the simultaneous operation of the excitation sources, equal to

$$S_T(\omega) = S_T^{(0)} = \frac{< \left|\hat{T}(\omega)\right|^2 >}{T_p} \tag{20}$$

where T_p is the time duration of the stochastic process and $\hat{T}(\omega)$ is the single realization of the temporal stochastic loading acting on both cantilevers and is equal to $\sqrt{S_T^{(0)}}\mathrm{e}^{\mathrm{i}\phi_T(\omega)}$, with $\phi_T(\omega)$ random phases uniformly distributed in the range from $-\pi$ to π.

Now, the input power spectral density matrix for the entire system can be defined as

$$\bar{\bar{\boldsymbol{S}}}_{FF} = C_0\bar{\bar{\mathbf{I}}} \tag{21}$$

where $\bar{\bar{\mathbf{I}}}$ is a $2N$ x $2N$ identity matrix and C_0, equal to $S_T^{(0)}S_X^{(0)}$, is only a scaling factor, which does not affect the shape of the system response and the correct evaluation of the quality factor resonator. Therefore, the output power spectral density matrix $\bar{\bar{\boldsymbol{S}}}_{UU}$ can be obtained as [52]

$$\bar{\bar{\boldsymbol{S}}}_{UU} = \bar{\bar{\boldsymbol{G}}}^*\bar{\bar{\boldsymbol{S}}}_{FF}\bar{\bar{\boldsymbol{G}}}^T = C_0\bar{\bar{\boldsymbol{G}}}^*\bar{\bar{\mathbf{I}}}\bar{\bar{\boldsymbol{G}}}^T \tag{22}$$

where

$$\bar{\bar{\boldsymbol{S}}}_{UU} = \begin{bmatrix} [\boldsymbol{S}_{U_1U_1}] & [\boldsymbol{S}_{U_1U_2}] \\ [\boldsymbol{S}_{U_2U_1}] & [\boldsymbol{S}_{U_2U_2}] \end{bmatrix}$$

In particular, the matrices of the autoPSD are

$$[\boldsymbol{S}_{U_1U_1}] = C_0\left([\boldsymbol{G}]_{11}^*[\boldsymbol{G}]_{11}^T + [\boldsymbol{G}]_{12}^*[\boldsymbol{G}]_{12}^T\right) \tag{23}$$

$$\left[\boldsymbol{S}_{U_2U_2}\right] = C_0\left([\boldsymbol{G}]^*_{22}[\boldsymbol{G}]^T_{22} + [\boldsymbol{G}]^*_{21}[\boldsymbol{G}]^T_{21}\right) \tag{24}$$

and, since $[\boldsymbol{G}]_{11} = [\boldsymbol{G}]_{22}$ and $[\boldsymbol{G}]_{12} = [\boldsymbol{G}]_{21}$ then $\left[\boldsymbol{S}_{U_1U_1}\right]$ is equal to $\left[\boldsymbol{S}_{U_2U_2}\right]$.

By performing the matrix product in Equation (22) on the entire chosen temporal frequency range and extracting the discrete autoPSD at the cantilever tip, we get

$$S_{U_iU_i}(L,\omega_k) = C_0\left(\sum_{s=1}^{N}|G_{ii}(L,\xi_s,\omega_k)|^2 + \sum_{s=1}^{N}|G_{ij}(L,\xi_s,\omega_k)|^2\right) \tag{25}$$

with $i,j = 1,2$ and $i \neq j,\ k = 1,\ldots,N_k$.

The computed description of the theoretical response requires the estimation of the fluid coefficient α and of the structural coupling stiffness k: this can be done by fitting the experimentally measured system response.

3. Experimental setup

The experimental setup adopted to completely assess the theoretical model is sketched in Figure 5. The QTF#S15, used in our experimental test campaign, is a custom QTF having prong length of 9.4 mm, width of 2.0 mm and crystal thickness of 0.25 mm. The prongs are spaced by 1.5 mm, [24,25], as reported in Table 1.

The QTF is excited in laboratory air by a stochastic, white acoustic field, generated by two speakers. The QTF response is measured by a LD Vibrometer. The experiments are carried out in static air at ambient temperature and atmospheric pressure: in these thermodynamic conditions the fluid kinematic viscosity is $\nu = 1.48 \times 10^{-5}\,\mathrm{m^2\,s^{-1}}$, while the density $\rho_f = 1.23\,\mathrm{kg\,m^{-3}}$. The setup is composed by: (i) a Polytec OFV-5000 modular LD vibrometer to measure the output response, in several points of the QTF, in terms of displacement and velocity, (ii) two speakers to produce a white acoustic random field for exciting the tuning fork structure, (iii) a Microtech Gefell 1/4" electret-measurement microphone M 370 to measure the acoustic pressure in proximity of the sensor, (iv) a LMS SCADAS Recorder 09 mobile PC based multichannel analyzer platform, running the LMS Test.Lab 14A software suite for generating the input electric signal to drive the speakers, and to acquire and record the time histories of the output responses measured by the vibrometer and the microphone. The adopted speakers' lay-out is sketched in Figure 5.

The base of the sensor is connected to a stationary frame through two welded tin masses. Therefore, the QTF device is modelled as fixed to the aforementioned frame by a bracket joint positioned on the base cross-section where the welded masses are located. The welded parts of the resonator are excluded from the geometry of the QTF used in the model (see Figure 6). Being the total length of the base plate equal to 5.1 mm part and excluding the welded part of 1.5 mm, a usable length of the base plate equal to 3.6 mm has been utilized in the calculations and reported as effective dimension in Table 1.

4. Results and discussion

In Figure 7, the autoPSD of the tip displacement of one prong is shown, in the frequency range from 14 to 17 kHz, which includes the first in-plane skew-symmetric flexural eigenfrequency of QTF#S15, approximately located at 15.8 kHz [24]. Three different peaks, located at 14.590 kHz, 15.808 kHz and 16.170 kHz were recorded in the experimental response: by performing an in-vacuum 3D finite element (FE) analysis of QTF#S15 by the software COMSOL, the three resonances are related

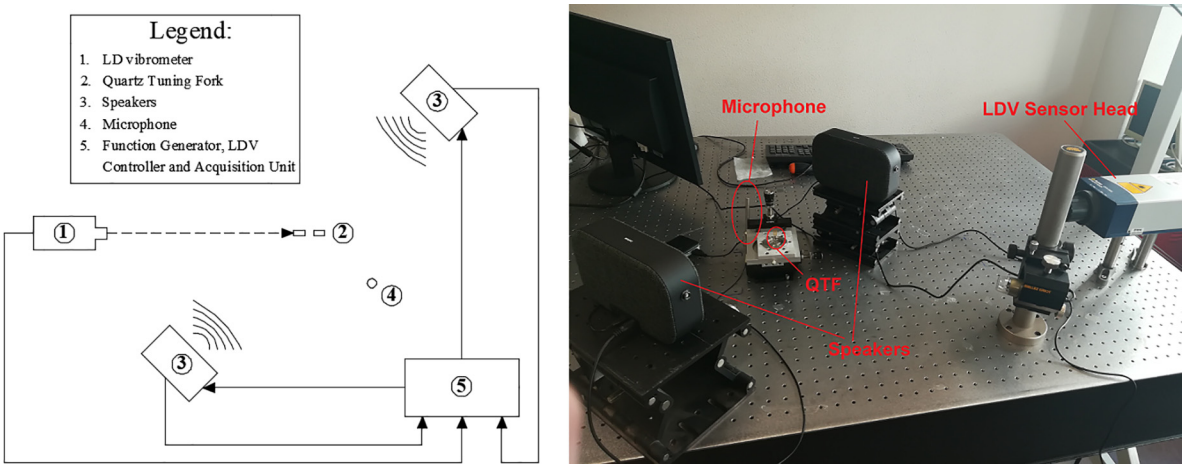

Fig. 5. Schematic representation of the adopted experimental setup (left panel) and the real experimental setup (right panel).

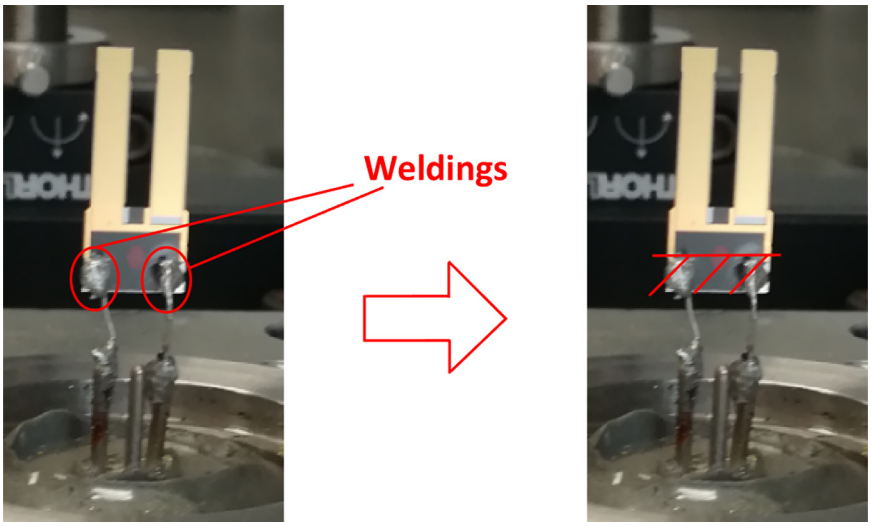

Fig. 6. Real-world constraint of the QTF sensor by two tin weldings (left panel) and adopted constraint by bracket joint (right panel).

to the first in-plane symmetric flexural mode, the first in-plane skew-symmetric flexural mode (the mode under investigation in this work, named hereafter as QEPAS mode), and to a torsional mode, having even out-of-plane displacement components, respectively. The finite element mode shapes and their relative eigenfrequencies compared with the experimental eigenfrequencies are depicted in the lower part of Figure 7.

As expected, owing to the adoption of a simple base-frame constraint model and since we are not considering any fluid-structure interaction in the FE simulation, a discrepancy between simulated values of FE eigenfrequencies and experimental peak frequencies is achieved. However, such a comparison between experimental outcomes and simplified FE results proves to be useful for identifying the mode type corresponding to each peak frequency included in the considered range. Besides, for the QEPAS mode, the relative error achieves an acceptable value, equal to 4%, due to the pure in-plane nature of such a mode. Such experimental outcomes can be modelled by employing the approach presented in Section 2 and, thus, performing numerical analyses aimed at computing the PSD of the QTF output response at its cantilever tips. In particular, we employed Equation (25), considering a spectral resolution $\Delta\omega = 2\pi \times 0.4\,\mathrm{rad\,s^{-1}}$, equal to that one used in the experiments, and a spatial discretization $\Delta x = \Delta\xi = 0.31\,\mathrm{mm}$. The added mass mainly causes shifts in the flexural in-plane skew-symmetric eigenfrequencies. However, it has been experimentally observed on several QTF geometries operating at very different air pressures (from 750 Torr to 25 Torr), that variations of air pressure surrounding the QTF causes slight shifts of resonance frequency and large variations of the hydrodynamic damping [22,23,33]. Thus, since the experiment is carried in open air, the added mass can be neglected. In fact, as anticipated, $\mu + \alpha\sqrt{\pi/2\omega} \ll \rho A(x)$, where $\mu + \alpha\sqrt{\pi/2\omega}$ is the real part of hydrodynamic function $\Gamma(\omega)$.

Then, a least squares fitting for all the remaining parameters can be performed: these include the diffusive-velocity coefficient α and the coupling stiffness k; furthermore, the scaling factor C_0 for the excitation source has to be properly set.

All assumed parameters and fitted values are listed in Table 2.

As a result, we obtain the theoretical response reported in Figure 8. In Figure 8, in the frequency range from 15.5 to 16.1 kHz, which includes the skew-symmetric eigenfrequency ω_{ss} of the QEPAS mode, we compare the experimental tip displacement autoPSD (red solid line) to that one resulting from the theoretical model $S_{U_iU_i}(L,\omega)$, computed, by using the Equation (25), when accounting for two different descriptions of the external force acting on the QTF cantilevers. In a first case, a perfectly white constant signal (green solid line) has been used as intensity of the temporal part of the external excitation in the Equation (25). In a second case, the acoustic pressure signal, measured by the microphone during the tests, has been employed as intensity of the temporal part of the external excitation (yellow solid line).

In Figure 8, we can conclude that experimental data can be satisfactorily fitted by the proposed theoretical model, with an R^2 of the theoretical fitted curve equal to 0.984. The quality factor value can be estimated by measuring the Full Width at Half Maximum (FWHM) value of the resonance curve [52]. As a result, an excellent match between measured and simulated Q-factor values is achieved, with a relative error with respect to the average experimental value, lower than 1%. We find

$$Q_{\mathrm{exp}} = \frac{\omega_{ss}}{\Delta\omega} = \frac{15808}{1.205} = 13119 \pm 1182.5$$

$$Q_{\mathrm{th}} = \frac{\omega_{ss}}{\Delta\omega} = \frac{15808}{1.203} = 13140$$

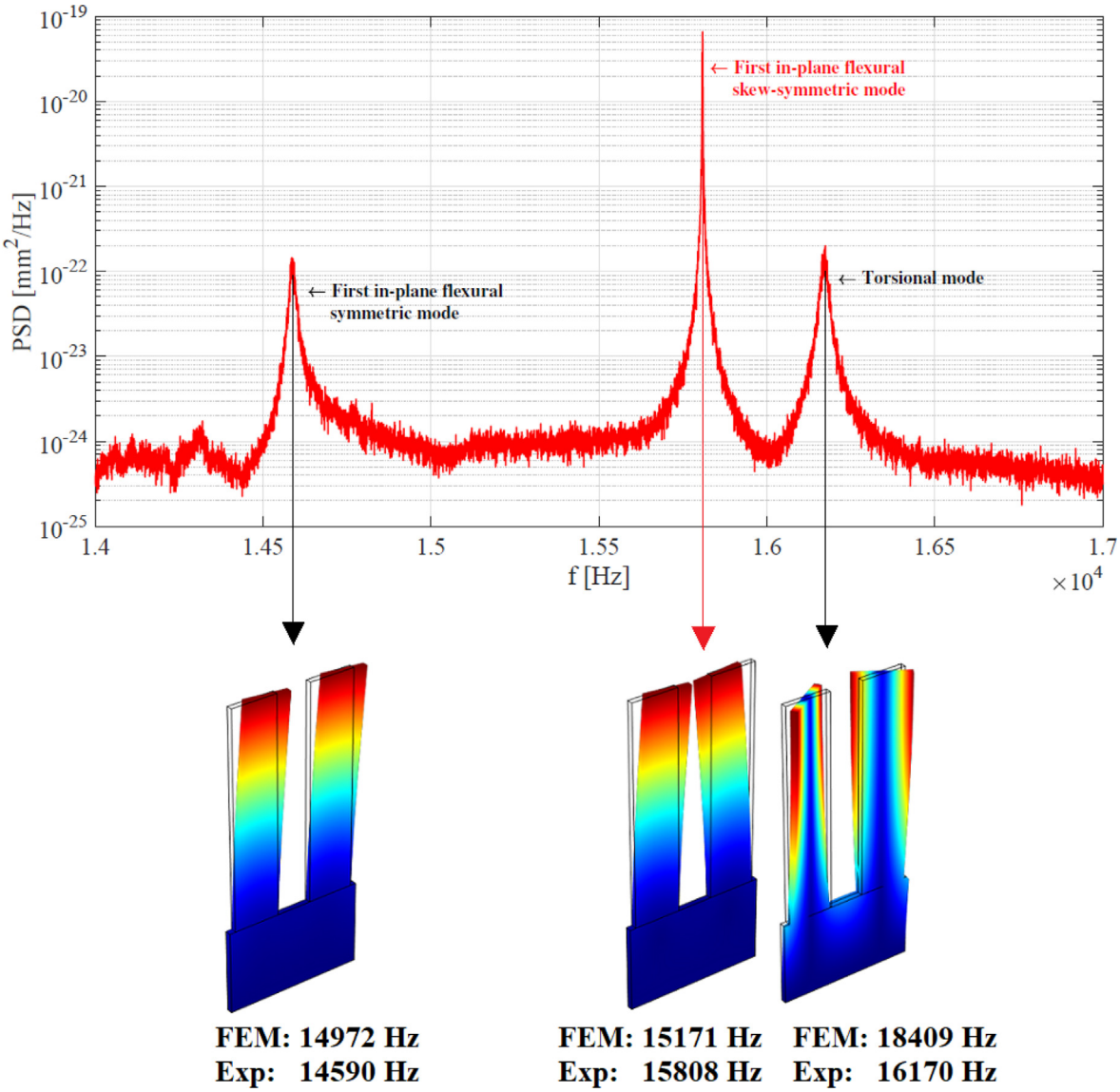

Fig. 7. The experimentally estimated autoPSD of the displacement measured at the tip of one QTF prong and the mode shape of each detected peak.

Table 2
Values of fluid model coefficient and structural coupling stiffness which fit the experimental response.

Fitting coefficients	α[Pa s$^{3/2}$]	k[Pa]
Values	2.341×10^{-5}	1.7865×10^{9}

Furthermore, let us observe that a specific aim of the approach presented in this paper is to enhance, in comparison with a traditional fluid-structure interaction FE model, the intelligibility of the physical parameters governing the dynamics of the phenomenon, in order to provide guidelines in designing of QTFs optimized for QEPAS gas sensing application. In particular, the very good agreement between the experimental data and the numerical fitting model confirms that, as assumed when formulating the hydrodynamic function, the system is dominated by a diffusive regime.

Therefore, let us focus on the analysis of the diffusive-velocity term. To this end, it is worth to point out that for the simple analytical case, shown previously in the Section 2.2, that is, for a plate vibrating in a viscous fluid in its own plane [44], it is possible to derive the analytical expression of the shear stress $\hat{\tau}_{zy}(x, y, \omega)$, exerted by the fluid on the surface, for a generic time law $u = u(t)$ of the moving surface, as

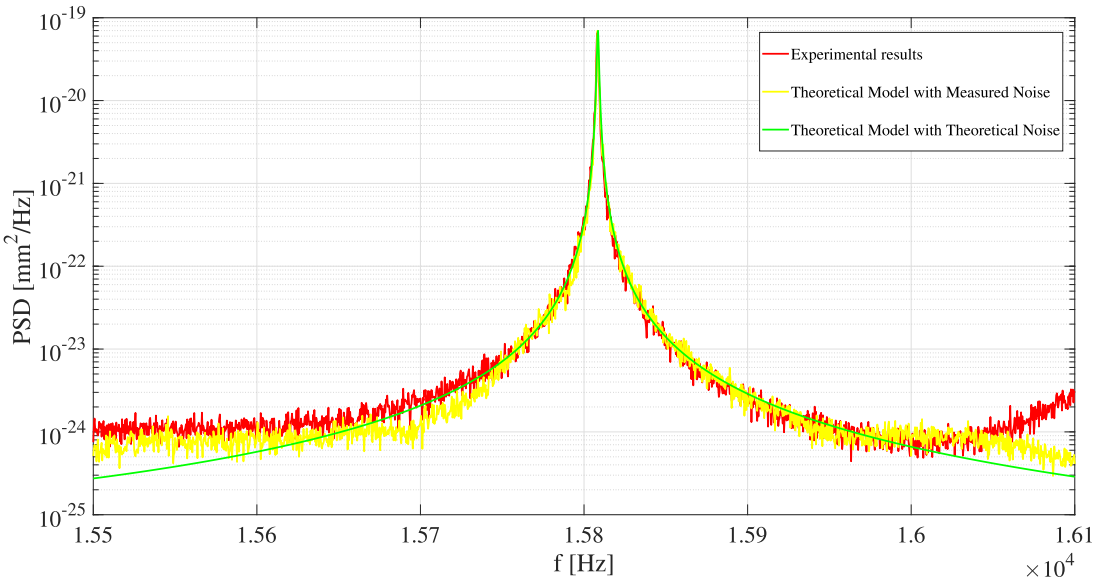

Fig. 8. Comparison between the simulated autoPSD of QTF tip displacement computed by using (i) the theoretically modelled external excitation (green curve) and (ii) the measured noise (yellow curve), and the experimental autoPSD of tip displacement (red curve). (For interpretation of the references to colour in this figure legend, the reader is referred to the web version of this article.)

$$\hat{\tau}_{zy}(x,y,\omega) = (1-\mathrm{i})\tilde{\alpha}\sqrt{\frac{\pi}{2}}\omega^{3/2}\hat{u}(\omega) \tag{26}$$

where the coefficient $\tilde{\alpha}$ is equal to $\tilde{\alpha} = \sqrt{\eta_f \rho_f / \pi}$. By applying this result to the case of the QTF#S15, and integrating the shear stress on both sides of the i-th cantilever, an analytical estimation α_L for the diffusive-velocity coefficient can be obtained as

$$\alpha_L = 2\,\tilde{\alpha}\left(\frac{L_b\frac{B}{2} + L_p b}{L}\right) = 1.21 \times 10^{-5}\,\mathrm{Pa\,s^{3/2}} \tag{27}$$

This is of the same order of magnitude of the value obtained by the implemented fitting procedure, thus, confirming the consistency of the performed estimation of the value for this parameter. Clearly, on a quantitative level, there exists a discrepancy between the analytical value of the diffusive coefficient α_L and the fitted one, due to edge and 3D effects of the fluid. Employing directly α_L to calculate the quality factor would lead to a potentially poor estimation, but the crucial physical point here is that the fluid dissipation for this case of a very thin tuning fork oscillating asymmetrically is completely characterized by the diffusive regime; identifying the fluid regime is extremely useful as it allows to reduce the number of parameters to fit and, thus, increase the physical intelligibility of the model. A more accurate estimation of α would need a larger analysis on different QTFs geometry in order to understand how this parameter can be related to the shape of the device. This is out of the scope of this paper, that is, to show the effectiveness of the proposed approach to model the dynamic response.

Now, another important parameter in the proposed model is the coupling stiffness k that is needed to model the structural coupling between the two prongs due to the underlying base plate of QTF device, the latter, in turn, gives rise to the skew-symmetric in-plane flexural QEPAS mode. It is worth pointing out that, by modelling the base plate as infinitely rigid body and studying the bending dynamics of each single fixed-free prong as a single Euler-Bernoulli beam, a single first in-plane flexural mode is obtained instead of a pair of symmetrical and skew-symmetrical ones. To account for both the modes, it is crucial to consider the structural coupling. Specifically, we observe that the frequency position of the skew-symmetric peak depends on k. While we have previously estimated the value of k by fitting the experimentally measured system response, now, in order to enhance the physical intelligibility of the model, we focus on how to obtain a physical value of k. The elastic behaviour of the base plate can be modelled as a continuous distribution of beams having infinitely small cross-section. In this case, all the beams will be subjected to only normal stresses, as depicted in Figure 9 and the axial stiffness of each beam can be calculated as

$$d\kappa = \frac{Eh}{g}dx \tag{28}$$

where g is the distance between the two cantilevers' axes, equal to $B/2$, as represented in Figure 9. Thus, the coupling stiffness per unit length $k = d\kappa/dx$ can be considered expressed by

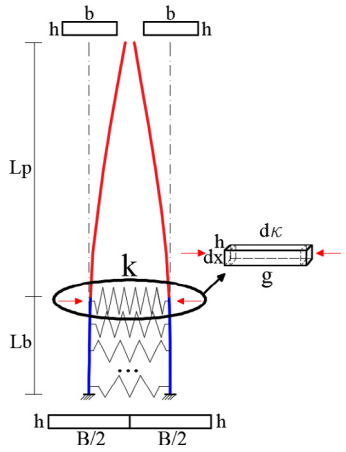

Fig. 9. Modelling of the elastic behaviour of the QTF inferior plate as a distribution of linear springs all subjected to only axial stress.

$$k = \frac{Eh}{g} \tag{29}$$

which decreases if the gap between the cantilevers is increased, as also confirmed in [20].

By using Equation (29), k is equal to $6 \times 10^9 \mathrm{N\,m^2}$, which is almost three times larger than the fitted value, as reported in Table 2. However, we have to consider that the corresponding skew-symmetric mode frequency is located at 16.694 kHz (see Figure 10), with a relative error of 5.6 % when compared to the actual frequency value equal to 15.808 kHz. This allows to conclude that even a rough estimation of the coupling stiffness k leads only to a small error on the QEPAS mode frequency, implying that the expression (29) can be suggested for improving the model predictivity. By using the estimated value of k, the frequency peak position slightly increases, but the shape and the FWHM value of the resonance curve remain almost the same, as shown in Figure 10, leading to a Q-factor characterized by an acceptable relative error of 4.3%, with respect to the experimental value $Q_{\mathrm{exp}} = 13119$, that is

$$Q_{\mathrm{th}}|_{k=Eh/g} = \frac{\omega_{ss}}{\Delta\omega} = \frac{16694}{1.22} = 13684 \approx Q_{\mathrm{exp}}$$

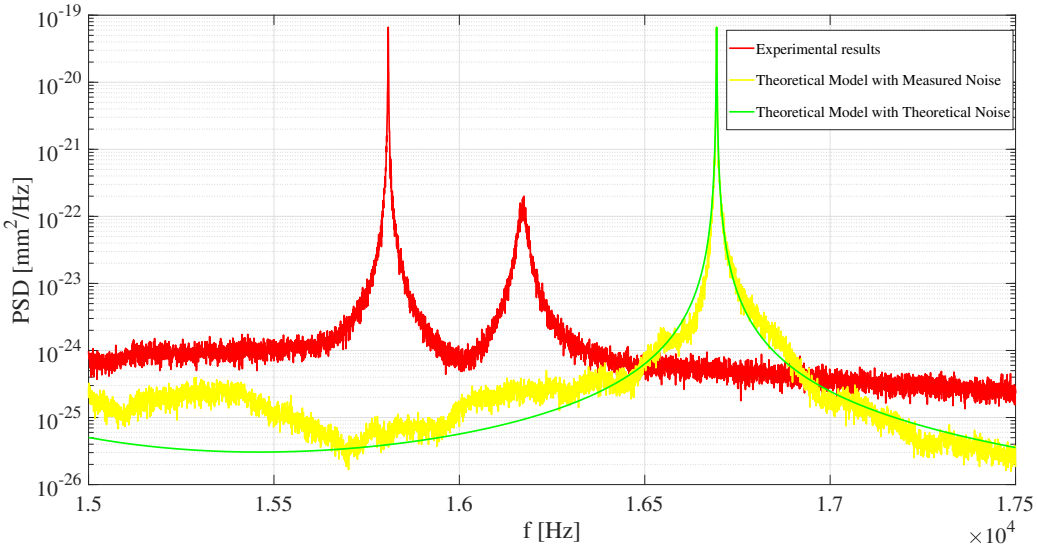

Fig. 10. Comparison between the simulated autoPSD of QTF tip displacement computed, in the case $k = Eh/g$, by using (i) the theoretically modelled external excitation (green curve) and (ii) the measured noise (yellow curve), and the experimental PSD of tip displacement (red curve). (For interpretation of the references to colour in this figure legend, the reader is referred to the web version of this article.)

5. Conclusion

In this work, we developed a numerical approach, relying on Boundary Element Methodology (BEM), to study the dynamic analysis of a quartz tuning fork (QTF) vibrating in a fluid environment. In detail, the quartz tuning fork has been modelled as a pair of Euler-Bernoulli cantilevers coupled by distributed linear springs with constant stiffness. The model takes into account the interaction between the QTF and the surrounding fluid. This is crucial for an accurate estimation of the quality factor of the first skew-symmetric in-plane flexural vibrational mode, corresponding to the specific mode at which the QTF is excited when employed as resonator in a QEPAS sensor. To this aim, an innovative analytical model of the fluid-structure interaction has been proposed, accounting for the inertial, the purely viscous and the diffusive terms. Due to the system linearity, the force exerted by the liquid on the body is the sum of these three contributions. Finally, the dynamic analysis of the problem has been reduced to the solution of an integral equation based on a properly defined Green's function, which takes into account the aforementioned terms, related to the fluid, and the elasticity of the two coupled beams. In comparison with a Finite Element approach, such an integrated strategy offers a high computational efficiency and the possibility of understanding how each parameter of the system influences the overall dynamic response.

In order to tune the model, a proper vibro-acoustic experimental setup has been implemented: the in-plane flexural vibration of a custom QTF immersed in air and excited by a white noise source have been acquired. The experimental data have been perfectly fitted by means of the proposed BEM-based model in a range of frequency close to the flexural mode typically excited in the QEPAS application, i.e. the first in-plane skew-symmetric flexural mode. By corroborating the theoretical model with experimental results, the effect of the diffusive-velocity term, originally derived by Landau [44] for the in-plane motion in a viscous fluid of an infinite half-space, and the effect of the structural coupling term have been analyzed and discussed. The first one is crucial to correctly estimate the system damping and, thus, the Q-factor; the second one, related to the structural coupling, is necessary to couple the two prongs and, thus, to be able to observe the skew-symmetric in-plane flexural mode. The value of the structural coupling stiffness affects only the position of the skew-symmetric peak and can be obtained by fitting the experimental data; alternatively, an approximate estimation of this value, based on theoretical considerations, leads to a still relatively good assessment of the skew-symmetric frequency and can make more predictive the model.

However, the proposed methodology requires an experimental fit for retrieving fluid coefficients and, in particular, for the α parameter, which marks the diffusive regime that governs the fluid-solid interaction. At the same time, it is crucial to underline that the proposed approach provides direct insights on the overall performance of the QTF and, more generally, can be considered a reliable procedure to analyze the fluid-structure interaction of a generic micro-electrical-mechanical device.

CRediT authorship contribution statement

A. Campanale: Conceptualization, Methodology, Validation, Formal analysis, Investigation, Resources, Writing - original draft, Writing - review & editing, Visualization. **C. Putignano:** Conceptualization, Methodology, Validation, Formal analysis, Investigation, Resources, Writing - review & editing, Visualization. **S. De Carolis:** Conceptualization, Methodology, Validation, Formal analysis, Investigation, Resources, Writing - review & editing, Visualization. **P. Patimisco:** Conceptualization, Investigation, Resources, Writing - review & editing, Visualization. **M. Giglio:** Conceptualization, Investigation, Resources, Writing - review & editing, Visualization. **L. Soria:** Conceptualization, Methodology, Validation, Formal analysis, Investigation, Resources, Writing - review & editing, Visualization.

Declaration of Competing Interest

The authors declare that they have no known competing financial interests or personal relationships that could have appeared to influence the work reported in this paper.

Acknowledgements

The authors thank Prof. Armenise and Prof. Ciminelli for providing access to experimental facilities in the Optoelectronics Laboratory at Polytechnic University of Bari, and Prof. Carbone and Prof. Spagnolo for the useful comments on the paper. Finally, the partial support of the Italian Ministry of Education, University and Research under the Programme Department of Excellence (Legge 232/2016 Grant No. CUP-D94I18000260001) is gratefully acknowledged.

Appendix A. Details of the solution scheme for the fundamental problem

Here, the fundamental problem, in which an impulsive force is applied to a section ξ of the bottom beam of the left cantilever, while the right one remains unloaded, is solved. We rewrite the set of Eqs. (12) for the fundamental problem, sketched in Figure 11, left panel, as

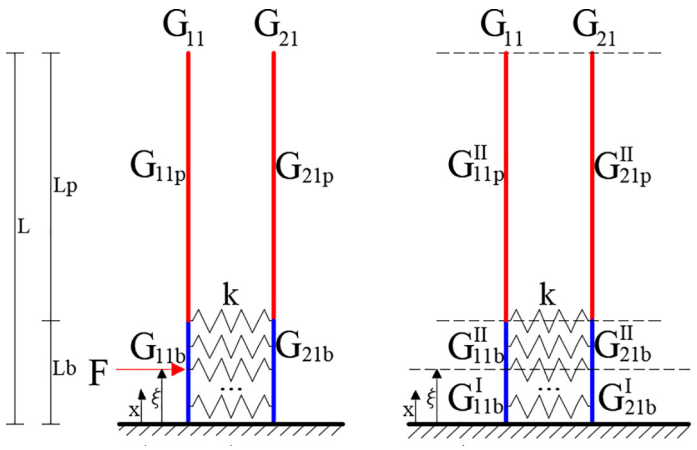

Fig. 11. 1D Euler-Bernoulli model of the fundamental problem. Fundamental problem with an impulsive force applied to a generic section ξ of the left cantilever (left panel), reduction of the fundamental problem to an homogeneous problem (right panel).

$$\frac{\partial^4 \overline{G}(x,\xi,\omega)}{\partial x^4} + \bar{\bar{B}}(x,\omega)\overline{G}(x,\xi,\omega) = \bar{f}(x,\xi,\omega) \tag{A.30}$$

where $\overline{G}(x,\xi,\omega) = \{G_{11}(x,\xi,\omega), G_{21}(x,\xi,\omega)\}^T$ and $\bar{f}(x,\xi,\omega) = \{\delta(x-\xi), 0\}^T$.

The x-dependence of $\bar{\bar{B}}(x,\omega)$ is due to the step discontinuity on the cross-section of the cantilevers at $x = L_b$ which makes the system of Equations (A.30) non-linear. However, this problem can be easily overcome by sub-splitting the solution $G_{11}(x,\xi,\omega)$ into $G_{11b}(x,\xi,\omega)$ and $G_{11p}(x,\xi,\omega)$ defined respectively for $0 < x < L_b$, depicted in blue in Figure 11, and for $L_b \leqslant x < L$, depicted in red; similarly for $G_{21}(x,\xi,\omega)$.

Therefore, the fundamental problem can be rewritten in the following form

$$\frac{\partial^4 \overline{G}(x,\xi,\omega)}{\partial x^4} + \bar{\bar{B}}(\omega)\overline{G}(x,\xi,\omega) = \bar{f}(x,\xi,\omega) \tag{A.31}$$

where $\overline{G}(x,\xi,\omega) = \{G_{11b}(x,\xi,\omega), G_{21b}(x,\xi,\omega), G_{11p}(x,\xi,\omega), G_{21p}(x,\xi,\omega)\}^T$, $\bar{f}(x,\xi,\omega) = \{\delta(x-\xi), 0, 0, 0\}^T$ and

$$\bar{\bar{B}}(\omega) = \begin{pmatrix} B_b(\omega) & -\frac{k}{EJ_b} & 0 & 0 \\ -\frac{k}{EJ_b} & B_b(\omega) & 0 & 0 \\ 0 & 0 & B_p(\omega) & 0 \\ 0 & 0 & 0 & B_p(\omega) \end{pmatrix}$$

with $B_b(\omega) = (1/EJ_b)\left(-\omega^2\left(\rho A_b - i\alpha\sqrt{\pi/2\omega}\right) + k\right)$ and $B_p(\omega) = (1/EJ_p)\left(-\omega^2\left(\rho A_p - i\alpha\sqrt{\pi/2\omega}\right)\right)$.

The set of Equations (A.31) is equivalent to the homogeneous problem depicted in Figure 11, right panel, that can be written as

$$\frac{\partial^4 \overline{G}(x,\xi,\omega)}{\partial x^4} + \bar{\bar{B}}(\omega)\overline{G}(x,\xi,\omega) = 0 \tag{A.32}$$

with $\overline{G}(x,\xi,\omega) = \left\{G^I_{11b}(x,\xi,\omega), G^I_{21b}(x,\xi,\omega), G^{II}_{11b}(x,\xi,\omega), G^{II}_{21b}(x,\xi,\omega), G^{II}_{11p}(x,\xi,\omega), G^{II}_{21p}(x,\xi,\omega)\right\}^T$ and

$$\bar{\bar{B}}(\omega) = \begin{pmatrix} B_b(\omega) & -\frac{k}{EJ_b} & 0 & 0 & 0 & 0 \\ -\frac{k}{EJ_b} & B_b(\omega) & 0 & 0 & 0 & 0 \\ 0 & 0 & B_b(\omega) & -\frac{k}{EJ_b} & 0 & 0 \\ 0 & 0 & -\frac{k}{EJ_b} & B_b(\omega) & 0 & 0 \\ 0 & 0 & 0 & 0 & B_p(\omega) & 0 \\ 0 & 0 & 0 & 0 & 0 & B_p(\omega) \end{pmatrix}$$

where the functions $G^I_{11b}(x,\xi,\omega)$ and $G^I_{21b}(x,\xi,\omega)$ are defined for $0 < x < \xi$, the functions $G^{II}_{11b}(x,\xi,\omega)$ and $G^{II}_{21b}(x,\xi,\omega)$ are defined for $\xi \leqslant x < L_b$ and the functions $G^{II}_{11p}(x,\xi,\omega)$ and $G^{II}_{21p}(x,\xi,\omega)$ are defined for $L_b \leqslant x < L$.

The set of Equations (A.32) comprises six coupled differential equations of fourth order needing the following 24 boundary conditions: fixed conditions at $x = 0$, continuity conditions at $x = \xi$, except for the third derivative of the solutions

$G^{I}_{11b}(x,\xi,\omega)$ and $G^{II}_{11b}(x,\xi,\omega)$ of the bottom-left beam since a concentrated force is applied to section ξ of the left cantilever, continuity conditions at $x = L_b$, and free-end conditions at $x = L$.

All the 24 boundary conditions are reported in detail at the end of this Appendix.

Next, we solve the associated eigenvalues problem [39] for the generic eigenvalue λ and the associated eigenvector $\mathbf{v}$, written as

$$\left(\bar{\bar{B}}(\omega) - \lambda(\omega)\bar{\bar{I}}_6\right)\mathbf{v} = 0 \tag{A.33}$$

where I_6 is the identity matrix of sixth order; then, we obtain the scaled modal matrix, as

$$\bar{\bar{\Psi}} = \begin{pmatrix} \frac{1}{\sqrt{2}} & \frac{1}{\sqrt{2}} & 0 & 0 & 0 & 0 \\ \frac{1}{\sqrt{2}} & -\frac{1}{\sqrt{2}} & 0 & 0 & 0 & 0 \\ 0 & 0 & \frac{1}{\sqrt{2}} & \frac{1}{\sqrt{2}} & 0 & 0 \\ 0 & 0 & \frac{1}{\sqrt{2}} & -\frac{1}{\sqrt{2}} & 0 & 0 \\ 0 & 0 & 0 & 0 & 1 & 0 \\ 0 & 0 & 0 & 0 & 0 & 1 \end{pmatrix}$$

It is worth to point out that the eigenvector $\left\{\frac{1}{\sqrt{2}}, \frac{1}{\sqrt{2}}, 0, 0, 0, 0\right\}^T$ corresponds to the symmetric vibration mode of the solutions $G^{I}_{11b}(x,\xi,\omega)$ and $G^{I}_{21b}(x,\xi,\omega)$, in which both cantilevers vibrate in phase with the same magnitude, and the eigenvector $\left\{0, 0, \frac{1}{\sqrt{2}}, \frac{1}{\sqrt{2}}, 0, 0\right\}^T$ corresponds to the symmetric vibration mode of the solutions $G^{II}_{11b}(x,\xi,\omega)$ and $G^{II}_{21b}(x,\xi,\omega)$, while the eigenvector $\left\{\frac{1}{\sqrt{2}}, -\frac{1}{\sqrt{2}}, 0, 0, 0, 0\right\}^T$ corresponds to the skew-symmetric vibration mode of the solutions $G^{I}_{11b}(x,\xi,\omega)$ and $G^{I}_{21b}(x,\xi,\omega)$, in which both cantilevers vibrate out of phase with the same magnitude, and the eigenvector $\left\{0, 0, \frac{1}{\sqrt{2}}, -\frac{1}{\sqrt{2}}, 0, 0\right\}^T$ corresponds to the skew-symmetric vibration mode of the solutions $G^{II}_{11b}(x,\xi,\omega)$ and $G^{II}_{21b}(x,\xi,\omega)$.

The modal matrix (5) allows for transforming the beam deflection field $\bar{G}$ to the modal coordinates $\bar{q}$, by means of the following relation

$$\bar{G} = \bar{\bar{\Psi}}\bar{q} \tag{A.34}$$

where $\bar{q} = \{q_1, q_2, q_3, q_4, q_5, q_6\}^T$ is the vector of the modal coordinates. By substituting (A.34) into (A.31) and premultiplying for $\bar{\bar{\Psi}}^T$, the Equation (A.31) can be rewritten in modal coordinates, as

$$\frac{\partial^4 \bar{q}(x,\xi,\omega)}{\partial x^4} + \lambda_i(\omega)\bar{\bar{I}}_6\bar{q}(x,\xi,\omega) = 0 \tag{A.35}$$

This is a system of six uncoupled fourth order partial differential equations, whose general solution can be written as

$$q_i(x,\xi,\omega) = a_i \cosh\left(\sqrt[4]{\lambda_i(\omega)}x\right) + a_{2i}\sinh\left(\sqrt[4]{\lambda_i(\omega)}x\right) + a_{3i}\cos\left(\sqrt[4]{\lambda_i(\omega)}x\right) + a_{4i}\sin\left(\sqrt[4]{\lambda_i(\omega)}x\right) \tag{A.36}$$

where a_i, a_{2i}, a_{3i} and a_{4i} for $i = 1, \ldots, 6$ are integration constants.

Once the solution is known in modal coordinates, it is possible to switch back to the physical coordinates by means of Equation (A.34) and numerically solve the set of 24 boundary conditions for fixed ξ and ω to obtain the 24 integration constants. The global susceptibility functions of the two cantilevers $G_{11}(x,\xi,\omega)$, for the left loaded cantilever, and $G_{21}(x,\xi,\omega)$, for the right not loaded cantilever, are given by piecewise functions, as

$$G_{11}(x,\xi,\omega) = \begin{cases} G^{I}_{11b}(x,\xi,\omega) & 0 < x < \xi \\ G^{II}_{11b}(x,\xi,\omega) & \xi < x < L_b \\ G^{II}_{11p}(x,\xi,\omega) & L_b < x < L \end{cases} \tag{A.37}$$

$$G_{21}(x,\xi,\omega) = \begin{cases} G^{I}_{21b}(x,\xi,\omega) & 0 < x < \xi \\ G^{II}_{21b}(x,\xi,\omega) & \xi < x < L_b \\ G^{II}_{21p}(x,\xi,\omega) & L_b < x < L \end{cases} \tag{A.38}$$

The fundamental problem can be similarly solved for an impulsive force applied to a different section ξ, in order to obtain the 3D matrices $[G]_{ij}$ for both cantilevers, as explained in subSection 2.4.

The boundary conditions for the homogeneous fundamental problem, Equation (A.32), are

- at $x = 0$

$$\begin{aligned} G^{I}_{11b}(0,\xi,\omega) &= \frac{\partial G^{I}_{11b}(x,\xi,\omega)}{\partial x}\Big|_{x=0} = 0 \\ G^{I}_{21b}(0,\xi,\omega) &= \frac{\partial G^{I}_{21b}(x,\xi,\omega)}{\partial x}\Big|_{x=0} = 0 \end{aligned} \tag{A.39}$$

- at $x = \xi$

$$\begin{aligned} G^{I}_{11b}(\xi,\xi,\omega) &= G^{II}_{11b}(\xi,\xi,\omega) \\ \frac{\partial G^{I}_{11b}(x,\xi,\omega)}{\partial x}\Big|_{x=\xi} &= \frac{\partial G^{II}_{11b}(x,\xi,\omega)}{\partial x}\Big|_{x=\xi} \\ \frac{\partial^2 G^{I}_{11b}(x,\xi,\omega)}{\partial x^2}\Big|_{x=\xi} &= \frac{\partial^2 G^{II}_{11b}(x,\xi,\omega)}{\partial x_2}\Big|_{x=\xi} \\ \frac{\partial^3 G^{II}_{11b}(x,\xi,\omega)}{\partial x^3}\Big|_{x=\xi} - \frac{\partial^3 G^{I}_{11b}(x,\xi,\omega)}{\partial x_3}\Big|_{x=\xi} &= 1 \\ G^{I}_{21b}(\xi,\xi,\omega) &= G^{II}_{21b}(\xi,\xi,\omega) \\ \frac{\partial G^{I}_{21b}(x,\xi,\omega)}{\partial x}\Big|_{x=\xi} &= \frac{\partial G^{II}_{21b}(x,\xi,\omega)}{\partial x}\Big|_{x=\xi} \\ \frac{\partial^2 G^{I}_{21b}(x,\xi,\omega)}{\partial x^2}\Big|_{x=\xi} &= \frac{\partial^2 G^{II}_{21b}(x,\xi,\omega)}{\partial x_2}\Big|_{x=\xi} \\ \frac{\partial^3 G^{II}_{21b}(x,\xi,\omega)}{\partial x^3}\Big|_{x=\xi} &= \frac{\partial^3 G^{I}_{21b}(x,\xi,\omega)}{\partial x_3}\Big|_{x=\xi} \end{aligned} \tag{A.40}$$

- at $x = L_b$

$$\begin{aligned} G^{II}_{11b}(L_b,\xi,\omega) &= G^{II}_{11p}(L_b,\xi,\omega) \\ \frac{\partial G^{II}_{11b}(x,\xi,\omega)}{\partial x}\Big|_{x=L_b} &= \frac{\partial G^{II}_{11p}(x,\xi,\omega)}{\partial x}\Big|_{x=L_b} \\ EJ_b \frac{\partial^2 G^{II}_{11b}(x,\xi,\omega)}{\partial x^2}\Big|_{x=L_b} &= EJ_p \frac{\partial^2 G^{II}_{11p}(x,\xi,\omega)}{\partial x^2}\Big|_{x=L_b} \\ EJ_b \frac{\partial^3 G^{II}_{11b}(x,\xi,\omega)}{\partial x^3}\Big|_{x=L_b} &= EJ_p \frac{\partial^3 G^{II}_{11p}(x,\xi,\omega)}{\partial x^3}\Big|_{x=L_b} \\ G^{II}_{21b}(L_b,\xi,\omega) &= G^{II}_{21p}(L_b,\xi,\omega) \\ \frac{\partial G^{II}_{21b}(x,\xi,\omega)}{\partial x}\Big|_{x=L_b} &= \frac{\partial G^{II}_{21p}(x,\xi,\omega)}{\partial x}\Big|_{x=L_b} \\ EJ_b \frac{\partial^2 G^{II}_{21b}(x,\xi,\omega)}{\partial x^2}\Big|_{x=L_b} &= EJ_p \frac{\partial^2 G^{II}_{21p}(x,\xi,\omega)}{\partial x^2}\Big|_{x=L_b} \\ EJ_b \frac{\partial^3 G^{II}_{21b}(x,\xi,\omega)}{\partial x^3}\Big|_{x=L_b} &= EJ_p \frac{\partial^3 G^{II}_{21p}(x,\xi,\omega)}{\partial x^3}\Big|_{x=L_b} \end{aligned} \tag{A.41}$$

- at $x = L_b + L_p = L$

$$\begin{aligned} \frac{\partial^2 G^{II}_{11p}(x,\xi,\omega)}{\partial x^2}\Big|_{x=L} &= \frac{\partial^3 G^{II}_{11p}(x,\xi,\omega)}{\partial x^3}\Big|_{x=L} = 0 \\ \frac{\partial^2 G^{II}_{21p}(x,\xi,\omega)}{\partial x^2}\Big|_{x=L} &= \frac{\partial^3 G^{II}_{21p}(x,\xi,\omega)}{\partial x^3}\Big|_{x=L} = 0 \end{aligned} \tag{A.42}$$

Appendix B. Estimation of the hydrodynamic function's coefficients by computational fluid dynamics finite element simulations.

Here, the values of coefficients c, α, and μ of hydrodynamic function $\Gamma(\omega)$, in Equation (9), are estimated by analysing, through computational fluid dynamics (CFD) simulations, the 2D unsteady Stokes' flow induced by the harmonic skew-symmetric oscillation, along the y-axis, of two identical rigid bodies, shaped as the prong cross-sections and immersed in an unbounded viscous incompressible medium. We, specifically, consider the fluid flow being 2D, since we hypothesize, as anticipated, the motion of cross-sections occurring in their yz-plane and the fluid velocity component along the cantilevers' x-axes being negligible.

The considered range of time frequencies is $\mathrm{f} \in \left[10^3, 10^5\right]$ Hz, in which five simulations per decade are performed. Each simulation is executed until the steady state of periodic regime is reached. The geometry of the computational domain along with the imposed boundary conditions is represented in Figure 12. By taking into account the geometric symmetry of the problem with respect to the motion y-direction and the further fluid dynamic symmetry with respect to the z-axis, due to the specific, considered out of phase oscillation, only one quarter of the whole domain is simulated. No-slip boundary conditions at the fluid-body interface and at the right edge of the computational domain are enforced; symmetry conditions are, thus, set along the left and bottom edges, while an open boundary condition is imposed at the top edge, as reported in Figure 12.

The problem is simulated by the finite element solver COMSOL Multiphysics, adopting a modeling technique based on the Laminar Flow (spf) and Moving Mesh (ale) physics interfaces. In particular, the P2 + P1 discretization is used, that is, piece-

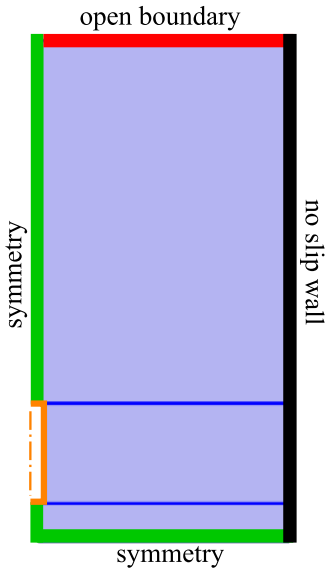

Fig. 12. Computational domain along with moving mesh regions and boundary conditions.

wise quadratic and linear interpolation, respectively, for velocity and pressure, combined with the default streamline diffusion and crosswind diffusion consistent stabilization methods, and with an extremely fine, physics-controlled moving mesh.

For each considered frequency value, by integration on the fluid-body interface, the time history of the force exerted by the fluid on the moving cross-section is computed. In particular, the y-component of these forces allows to extract the amplitude and the phase lag of the hydrodynamic function $\Gamma(\omega)$ with respect to the imposed displacement by Equation (8). It is worth pointing out that, in case of unsteady Stokes' flow and, thus, oscillations of small amplitude, owing to the linearity of the problem, the computed force time histories are harmonic signals at the same radian frequency ω of the imposed movement.

The requisite values of coefficients c, α, and μ, are collected in Table 3 and estimated by implementing a specific nonlinear fitting strategy of achieved numerical results, relying on the approximate expression Equation (9) of the hydrodynamic function $\Gamma(\omega)$. By adopting a purely diffusive model of the imaginary part of the hydrodynamic function, i.e. by assuming $c = 0$ Pa s, we estimate, for the sole diffusive-velocity coefficient, the value $\alpha = 1.70 \times 10^{-5}$ Pa s$^{3/2}$. We point out that the observed discrepancy between the experimental value of the coefficient and that obtained by the numerical procedure here reported is related to the ensemble of effects which have been neglected, as well as to the measurements' uncertainties.

In Figure 13, the real and the imaginary parts of the hydrodynamic function $\Gamma(\omega)$ are shown, evaluated by the approximate expression Equation (9) and computed by using the fitted values of the coefficients c, α, and μ, collected in Table 3. By even representing the single summands $\mu, \alpha\sqrt{\pi/(2\omega)}$, and c/ω, and highlighting the QEPAS mode frequency location, it is clearly possible to see, from the analysis of imaginary part, that the linear viscous damping term is basically negligible, with respect to the importance of the diffusive-velocity term, as expected, given the small difference between the α fitted values with $c \neq 0$ Pa s or $c = 0$ Pa s. Given, moreover, the negligible importance of mass adding, as also expected and testified by the experimental results presented in Refs. [22–33], it is straightforward to conclude that the two conditions $c\omega^{-1} \ll \alpha\sqrt{\pi/2\omega}$ and $\mu + \alpha\sqrt{\pi/2\omega} \ll \rho A(x)$ describe the purely α-driven regime which characterizes the QTF forced vibration at the QEPAS frequency.

We consider useful to stress that only one hydrodynamic function is sufficient to describe the hydrodynamic coupling between the two cantilevers vibrating at the QEPAS resonance frequency. In fact, while in Ref. [39], it is proven that two independent hydrodynamic functions are needed to thoroughly identify the system dynamics in each possible coupling condition, in case of skew-symmetric vibration, here under investigation, given the same motion amplitude of the bodies, only one function describes the specific situation, which corresponds to a simple linear combination of the two above recalled

Table 3
Values of fluid model coefficients which fit the CFD numerical results.

Fitting coefficients	c[Pa s]	α[Pa s$^{3/2}$]	μ[Pa s^2]
Values	9.88×10^{-5}	1.62×10^{-5}	1.36×10^{-7}

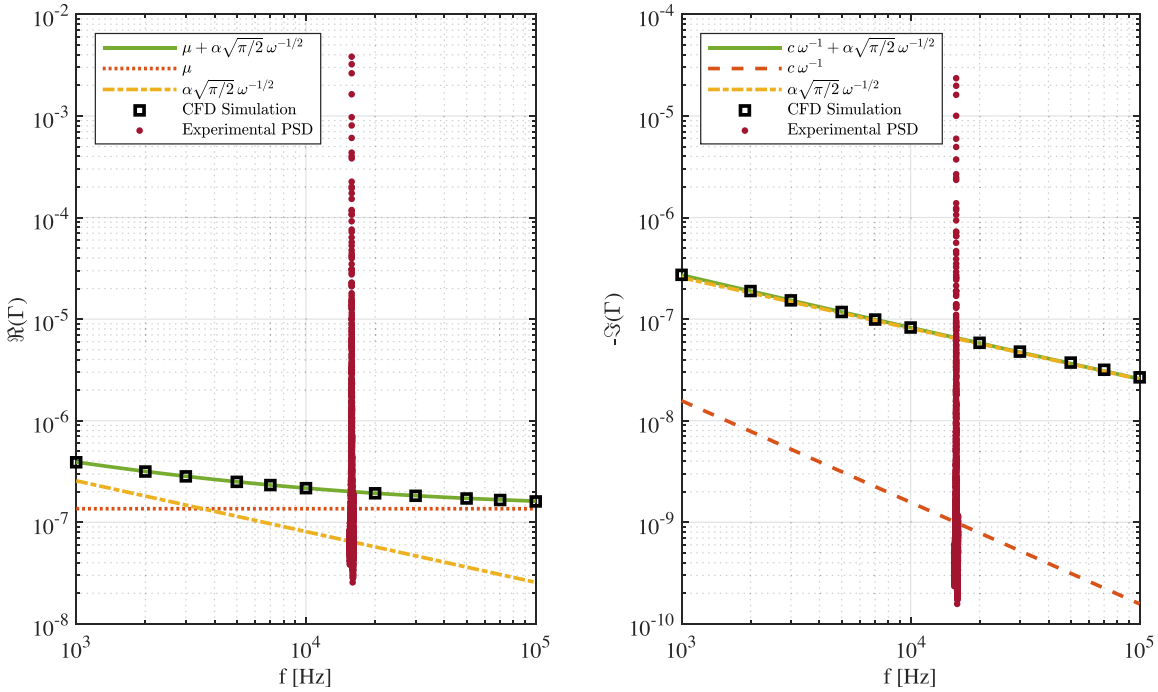

Fig. 13. Real and imaginary parts of hydrodynamic function $\Gamma(\omega)$. Comparison between approximate expression (9) evaluated with fitted coefficients collected in Table 3 (solid line) and CFD numerical results (squared markers). Single summands μ (dotted line), $\alpha\sqrt{\pi/(2\omega)}$ (dotted-dashed line), and c/ω (dashed line) of real and imaginary part are represented to elucidate their relative importance. The experimentally estimated PSD (solid dots) is reported to highlight the frequency location of the first QTF skew-symmetric in-plane flexural mode.

independent functions. Therefore, α-values here estimated account for the hydrodynamic coupling existing between the two oscillating cantilevers.

References

[1] J. Hodgkinson, R.P. Tatam, Optical gas sensing: a review, Meas. Sci. Technol. 24 (1) (2013), 012004.
[2] P. Daukantas, Air-quality monitoring in the mid-infrared, Opt. Photonics News 26 (11) (2015) 26–33.
[3] L. Zhang, G. Tian, J. Li, B. Yu, Applications of absorption spectroscopy using quantum cascade lasers, Appl. Spectrosc. 68 (2014) 1095–1107.
[4] M. Jahjah, W. Jiang, N.P. Sanchez, W. Ren, P. Patimisco, V. Spagnolo, S.C. Herndon, R.J. Griffin, F.K. Tittel, Atmospheric CH4 and N2O measurements near Greater Houston area landfills using a QCL based QEPAS sensor system during DISCOVER-AQ 2013, Opt. Lett. 39 (2014) 957–960.
[5] A. Sampaolo, S. Csutak, P. Patimisco, M. Giglio, G. Menduni, V. Passaro, F.K. Tittel, M. Daffenbaugh, V. Spagnolo, Methane, ethane and propane detection using a compact quartz enhanced photoacoustic sensor and a single interband cascade laser, Sensors Actuators B: Chemical 282 (2019) 952–960.
[6] J. Mikołajczyk, Z. Bielecki, T. Stacewicz, J. Smulko, J. Wojtas, D. Szabra, L. Lentka, A. Prokopiuk, P. Magryta, Detection of gaseous compounds with different techniques, Metrology Measure. Syst. 23 (2016) 205–224.
[7] A.G. Bell, On the production and reproduction of sound by light, Am. J. Sci. 20 (1880) 305.
[8] A.G. Bell, Upon the production of sound by radiant energy, Philos. Mag. 11 (1881) 510.
[9] Y.H. Pao, Optoacoustic Spectroscopy and Detection, Academic, New York, 1977.
[10] S. Schäfer, A. Miklos, P. Hess, Progress in Photothermal and Photoacoustic Science and Technology (SPIE, Bellingham, WA, 1997), Vol. III.
[11] A.A. Kosterev, Y.A. Bakhirkin, R.F. Curl, F.K. Tittel, Quartz-enhanced photoacoustic spectroscopy, Opt. Lett. 27 (21) (2002) 1902–1904.
[12] A.A. Kosterev, F.K. Tittel, D.V. Serebryakov, A.L. Malinovsky, I.V. Morozov, Applications of quartz tuning forks in spectroscopic gas sensing, Rev. Sci. Instrum. 76 (2005), 043105.
[13] A. Elia, P.M. Lugarà, C.D. Franco, V. Spagnolo, Photoacoustic Techniques for Trace Gas Sensing Based on Semiconductor Laser Sources, Sensors 9 (2009) 9616–9628.
[14] P. Patimisco, A. Sampaolo, L. Dong, F.K. Tittel, V. Spagnolo, Recent advances in quartz enhanced photoacoustic sensing, Appl. Phys. Rev. 5 (2018), 011106.
[15] S. Borri, P. Patimisco, A. Sampaolo, H.E. Beere, D.A. Ritchie, M.S. Vitiello, G. Scamarcio, V. Spagnolo, Terahertz quartz enhanced photo-acoustic sensor, Appl. Phys. Lett. 103 (2013) 02110.
[16] P. Patimisco, G. Scamarcio, V. Spagnolo, Quartz-enhanced photoacoustic spectroscopy: a review, Sensors 4 (2014) 6165–6206.
[17] P. Patimisco, A. Sampaolo, H. Zheng, L. Dong, F.K. Tittel, V. Spagnolo, Quartz enhanced photoacoustic spectrophones exploiting custom tuning forks: a review, Adv. Phys. X 2 (2017) 169–187.
[18] T.D. Rossing, D.A. Russell, D.E. Brown, On the acoustics of tuning forks, Am. J. Phys. 60 (1992) 620–626.
[19] L. Soria, E. Pierro, G. Carbone, T. Contursi, Tuning fork microgyrometers: narrow gap vs. wide gap design, Journal of Sound and Vibrations 322 (1–2) (2009) 78–97.
[20] E.G. Santos, D. Ramos, V. Pini, M. Calleja, J. Tamayo, Exponential tuning of the coupling constant of coupled microcantilevers by modifying their separation Appl, Phys. Lett. 98 (2011), 123108.
[21] M. Napoli, W. Zhang, K. Turner, Characterization of Electrostatically Coupled Microcantilevers, J. Microelectromechanical Syst. 14 (2) (2005) 295.
[22] P. Patimisco, A. Sampaolo, L. Dong, M. Giglio, G. Scamarcio, F.K. Tittel, V. Spagnolo, Analysis of the electro-elastic properties of custom quartz tuning forks for optoacoustic gas sensing, Sensors Actuators B: Chemical 227 (2016) 539–546.

[23] P. Patimisco, S. Borri, A. Sampaolo, H.E. Beere, D.A. Ritchie, M.S. Vitiello, G. Scamarcio, V. Spagnolo, A quartz enhanced photo-acoustic gas sensor based on a custom tuning fork and a terahertz quantum cascade laser, Sensors Actuators B: Chemical 139 (2014) 2079.
[24] P. Patimisco, A. Sampaolo, M. Giglio, S. Dello Russo, V. Mackowiak, H. Rossmadl, A. Cable, F.K. Tittle, V. Spagnolo, Tuning forks with optimized geometries for quartz-enhanced photoacoustic spectroscopy, Opt. Express 27 (2019) 1401–1415.
[25] S. Dello Russo, M. Giglio, A. Sampaolo, P. Patimisco, G. Menduni, H. Wu, L. Dong, V.M.N. Passaro, V. Spagnolo, Acoustic Coupling between Resonator Tubes in Quartz-Enhanced Photoacoustic Spectrophones Employing a Large Prong Spacing Tuning Fork, Sensors 19 (19) (2019) 4109.
[26] F.R. Blom, S. Bouwstra, M. Elwenspoek, J.H.J. Fluitman, Dependence of the quality factor of micromachined silicon beam resonators on pressure and geometry, J. Vac. Sci. Technol. B 10 (1992) 19.
[27] H. Hosaka, K. Itao, S. Kuroda, Damping characteristics of beam-shaped micro-oscillators, Sensors Actuators A: Physical 49 (1995) 87–95.
[28] K. Kokubun, H. Murakami, Y. Toda, M. Ono, A bending and stretching mode crystal oscillator as a friction vacuum gauge, Vacuum 34 (1984) 731–735.
[29] Y. Jimbo, K. Itao, Energy loss of a cantilever vibrator, J. Horological Inst. Jpn 47 (1968) 1.
[30] D.M. Photiadis, J.A. Judge, Attachment losses of high Q oscillators, Appl. Phys. Lett. 85 (2005) 482.
[31] Z. Hao, A. Erbil, F. Ayazi, An analytical model for support loss in micromachined beam resonators with in-plane flexural vibrations, Sensors Actuators A: Physical 109 (2003) 156–164.
[32] C. Zener, Internal friction in solids II. General theory of thermoelastic internal friction, Phys. Rev. 53 (1938) 90–99.
[33] M. Giglio, G. Menduni, P. Patimisco, A. Sampaolo, A. Elefante, V.M.N. Passaro, V. Spagnolo, Damping Mechanisms of Piezoelectric Quartz Tuning Forks Employed in Photoacoustic Spectroscopy for Trace Gas Sensing, Phys. Status Solidi A 216 (2019) 1800552.
[34] P. Patimisco, A. Sampaolo, V. Mackowiak, H. Rossmadl, A. Cable, F.K. Tittel, V. Spagnolo, Loss Mechanisms Determining the Quality Factors in Quartz Tuning Forks Vibrating at the Fundamental and First Overtone Modes, IEEE Trans. Ultrasonics, Ferroelectrics, Frequency Control 65 (10) (2018).
[35] S. Inceloglu, M. Gurgoze, Bending vibrations of beams coupled by a double spring-mass system, J. Sound Vib. 243 (2) (2001) 361–369.
[36] R.J. Clarke, O.E. Jensen, J. Billingham, A.P. Pearson, P.M. Williams, Phys. Rev. Lett 96 (2006), 050801.
[37] R.J. Clarke, S.M. Cox, P.M. Williams, O.E. Jensen, J. Fluid. Mech. 545 (2005) 397.
[38] J.E. Sader, J. Appl. Phys 84 (1998) 64.
[39] C. Intartaglia, L. Soria, M. Porfiri, Hydrodynamic coupling of two sharp-edged beams vibrating in a viscous fluid, Proc. R. Soc. A: Math., Phys. Eng. Sci. 470 (2162) (2014) 20130397.
[40] F. Cellini, C. Intartaglia, L. Soria, M. Porfiri, Effect of hydrodynamic interaction on energy harvesting in arrays of ionic polymer metal composites vibrating in a viscous fluid, Smart Mater. Struct. 23 (4) (2014), 045015.
[41] E. Grimaldi, M. Porfiri, L. Soria, Finite amplitude vibrations of a sharp-edged beam immersed in a viscous fluid near a solid surface, J. Appl. Phys. 112 (10) (2012), 104907.
[42] C.Y. Wang, Exact solutions of the steady-state Navier-Stokes equations, Ann. Rev. Fluid Mech. 23 (1991) 159–177.
[43] Y. Zeng, S. Weinbaum, Stokes problems for moving half-planes, J. Fluid Mech. 287 (1995) 59–74.
[44] L.D. Landau, E.M. Lifshitz, Fluid Mechanics, 2nd ed., PergamonPress, 1984.
[45] R. Cox, J. Zhang, F. Josse, S.M. Heinrich, I. Dufour, L.A. Beardslee, O. Brand, Damping and mass sensitivity of laterally vibrating resonant microcantilevers in viscous liquid media, Proc. IEEE Int. Frequency Control Symposium Exposition (2011).
[46] R. Cox, J. Zhang, F. Josse, S.M. Heinrich, O. Brand, I. Dufour, Characteristics of laterally vibrating resonant microcantilevers in viscous liquid media, J. Appl. Phys. 111 (1) (2012), 014907.
[47] E. Pierro, F. Bottiglione, G. Carbone, Thermal fluctuations and dynamic modelling of a dAFM cantilever, Adv. Theory Simul. 2 (5) (2019) 1900004.
[48] Y. Bazilevs, K. Takizawa, T.E. Tezduyar, Computational fluid-structure interaction: methods and applications, John Wiley & Sons, 2013.
[49] P.K. Banerjee, P.K. Banerjee, R. Butterfield, Boundary element methods in engineering science, (McGraw-Hill Book Co, 1981.
[50] C. Putignano, G. Carbone, D. Dini, Theory of reciprocating contact for viscoelastic solids, Phys. Rev. E 93 (4) (2016), 043003.
[51] C. Putignano, Soft lubrication: a generalized numerical methodology, J. Mech. Phys. Solids 134 (2020), 103748.
[52] L. Meirovitch, Fundamentals of Vibrations, McGraw-Hill, 1975.
[53] C. Putignano, J. Le Rouzic, T. Reddyhoff, G. Carbone, D. Dini, A theoretical and experimental study of viscoelastic rolling contacts incorporating thermal effects, Proceedings of the Institution of Mechanical Engineers, Part J: Journal of Engineering Tribology (2014), https://doi.org/10.1177/1350650114530681.